Generalized Minimum-Error Thresholding for Unsupervised Change Detection From SAR Amplitude Imagery

Gabriele Moser, *Member, IEEE*, and Sebastiano B. Serpico, *Senior Member, IEEE*

Abstract—The availability of synthetic aperture radar (SAR) data offers great potential for environmental monitoring due to the insensitiveness of SAR imagery to atmospheric and sunlight-illumination conditions. In addition, the short revisit time provided by future SAR-based missions will allow a huge amount of multitemporal SAR data to become systematically available for monitoring applications. In this paper, the problem of detecting the changes that occurred on the ground by analyzing SAR imagery is addressed by a completely unsupervised approach, i.e., by developing an automatic thresholding technique. The image-ratioing approach to SAR change detection is adopted, and the Kittler and Illingworth minimum-error thresholding algorithm is generalized to take into account the non-Gaussian distribution of the amplitude values of SAR images. In particular, a SAR-specific parametric modeling approach for the ratio image is proposed and integrated into the thresholding process. Experimental results, which confirm the accuracy of the method for real X-band SAR and spaceborne imaging radar C-band images, are presented.

Index Terms—Change detection, Kittler and Illingworth method, method of log-cumulants (MoLC), parametric density estimation, synthetic aperture radar (SAR), thresholding.

I. INTRODUCTION

REMOTELY sensed imagery of a geographical area of interest represents a precious source of information for environmental monitoring applications (e.g., land-use and land-cover dynamic analysis, crop monitoring, and deforestation studies). In particular, the availability of synthetic aperture radar (SAR) data provides great potential from this viewpoint due to the insensitiveness of SAR sensors to atmospheric (in particular, rain and clouds) and sunlight-illumination conditions [1]. In addition, due to the short revisit time provided by future SAR-based missions (e.g., COSMO/SkyMed, TerraSAR, or PALSAR with pointing functionality), a huge amount of multitemporal SAR data is expected to become systematically available for monitoring applications. Hence, multitemporal SAR imagery is expected to play an important role, for instance, in the context of ecological applications [2] or in disaster assessment and prevention [3], [4]. In particular, image-processing techniques that allow one to detect the changes that occurred in a given monitored area between successive acquisition dates may represent efficient data-analysis tools.

Several approaches have been proposed in the literature to deal with change detection, such as image ratioing [1], multitemporal coherence analysis [5], integration of segmentation

with multilayer perceptron and Kohonen neural networks [6], fuzzy-rule-based analysis [7], multisource (optical and SAR) and multitemporal data fusion [8], spatiotemporal contextual classification [9], [10], and likelihood ratio tests [11], [12].

In this paper, the problem of SAR-based change detection is addressed in a completely unsupervised way, which assumes no training data to be available at any observation date. The adopted image-ratioing approach generates a ratio image by dividing pixel-by-pixel the gray levels at one date by the gray levels at another date. Similar to the image differencing for change detection in optical data [13], SAR image ratioing involves the critical problem of the selection of an optimal threshold value to be applied to the ratio image to separate "change" from "no-change." "Trial-and-error" procedures are typically adopted to this end [1], [13]–[15]. However, such manual operations typically turn out to be time consuming; in addition, the quality of their results critically depends on the visual interpretation of the user.

In this paper, the problem of automating the threshold-selection task is addressed by proposing an unsupervised technique that integrates image ratioing with a generalization of the Kittler and Illingworth minimum-error thresholding algorithm (K&I) [16]. The change-detection method (proposed in [17] and [18] with regard to optical imagery) that integrates K&I with image differencing is modified by developing a new version of K&I, which is suited to image ratioing and to the specific non-Gaussian statistics of SAR amplitude ratio images. In particular, three versions of the resulting method that differ in the specific parametric models postulated for the change and the no-change hypotheses (i.e., the "Nakagami-ratio," the "Weibull-ratio," and the log-normal models; see Sections II-C–E) are developed and endowed with suitable parameter-estimation algorithms based on the method of log-cumulants (MoLC), which is recently introduced in the specific context of SAR data modeling [19], [20].

The novelty of the algorithm proposed in this paper lies in several aspects. First, innovative elements are represented by the automatization of the thresholding process for SAR change detection by the corresponding non-Gaussian generalization of K&I and by the integration of MoLC into the K&I framework. Moreover, the formulation of the Weibull-ratio model, which is obtained by ratioing two independent Weibull-distributed SAR amplitudes (see Section II-E), and the development of the MoLC estimation strategy for the Nakagami-ratio and Weibull ratio conditional models (see Sections II-C and E, respectively) are proposed in this paper and turn out to be innovative. It is worth noting that a similar K&I-based approach to SAR change detection has very recently been adopted in [21],

although operating on the log-ratio (and not ratio) image and using a completely different model and parametric-estimation technique for the class statistics (i.e., a generalized Gaussian (GG) model for the change and no-change classes in the log-ratio image, following a moment-based estimation method).

In Section II, the proposed change-detection methodology is derived, and the related parametric probability density function (pdf) estimation issues are discussed. Section III reports on the results of the application of the proposed approach to real multitemporal X-band Synthetic Aperture Radar (XSAR) and Spaceborne Imaging Radar C-band (SIR-C) imagery, as compared with the results obtained by an exhaustive search for the optimal threshold for the considered test set. Finally, conclusions are drawn in Section IV.

II. METHODOLOGY

A. K&I

Given a generic single-band (i.e., scalar) image $\mathcal{I} = \{z_1, z_2, \ldots, z_N\}$, which is modeled as a set of independent identically distributed (i.i.d.) random variables with pdf p_z, K&I addresses the problem of splitting the image data as a two-category classification problem [22] by an unsupervised thresholding approach and allows to compute automatically a threshold value that aims at minimizing the probability of classification error [16]. Hence, denoting by H_0 and H_1 the two hypotheses to be distinguished and by τ the threshold, the kth pixel is assigned to H_0 if $z_k \leq \tau$ and to H_1 if $z_k > \tau$ ($k = 1, 2, \ldots, N$).

K&I assumes a parametric Gaussian model $\mathcal{N}(m_i, \sigma_i^2)$ characterized by the mean m_i and by the variance σ_i^2 for the pdf of a gray level z_k ($k = 1, 2, \ldots, N$) under each hypothesis H_i ($i = 0, 1$). Denoting such a pdf by $p_i(\cdot|m_i, \sigma_i)$ and the prior probability of each hypothesis H_i by $P_i = P(H_i)$ ($i = 0, 1$), K&I expresses the unsupervised threshold-selection problem as the minimization of a criterion function $J(\tau)$ related to the Bayes decision rule for the minimum classification error (i.e., the "maximum *a posteriori*" (MAP) rule) [22]. In particular, by assuming the gray levels in $\mathcal{I}$ to be quantized into Z levels $\{0, 1, \ldots, Z - 1\}$ and by denoting by $\{h(z) : z = 0, 1, \ldots, Z - 1\}$ the (normalized) histogram of $\mathcal{I}$, the criterion function is computed by averaging a cost function $c(z, \tau)$ that quantifies the cost of labeling a pixel by comparing its gray level z with threshold τ [16]. A histogram-based estimate of the expectation $E\{c(z, \tau)\}$ is used, which is obtained by estimating the unconditional pdf p_z of the gray levels with the image histogram, i.e.,

$$J(\tau) = \sum_{z=0}^{Z-1} h(z) c(z, \tau). \tag{1}$$

K&I introduces the following histogram-based estimates (parameterized by τ) of the parameters P_i, m_i, and σ_i of each hypothesis $H_i (i = 0, 1)$:

$$\hat{P}_{i\tau} = \sum_{z \in R_{i\tau}} h(z)$$

$$\hat{m}_{i\tau} = \frac{\sum_{z \in R_{i\tau}} z h(z)}{\sum_{z \in R_{i\tau}} h(z)}$$

$$\hat{\sigma}_{i\tau}^2 = \frac{\sum_{z \in R_{i\tau}} h(z)(z - \hat{m}_{i\tau})^2}{\sum_{z \in R_{i\tau}} h(z)} \tag{2}$$

where

$$R_{0\tau} = \{0, 1, \ldots, \tau\} \quad R_{1\tau} = \{\tau + 1, \tau + 2, \ldots, Z - 1\} \tag{3}$$

are the sets of levels assigned to H_0 and H_1, respectively [16], and can be interpreted as the two related decision regions. As the method aims at minimizing the probability of classification error, the following expression (up to additive or multiplicative constants) is chosen for the cost function [16]:

$$c(z, \tau)$$

$$= \begin{cases} -\ln \hat{P}_{0\tau} - \ln p_0(z|\hat{m}_{0\tau}, \hat{\sigma}_{0\tau}) & \text{for } z = 0, 1, \ldots, \tau \\ -\ln \hat{P}_{1\tau} - \ln p_1(z|\hat{m}_{1\tau}, \hat{\sigma}_{1\tau}) & \text{for } z = \tau + 1, \tau + 2, \\ & \qquad \ldots, Z - 1. \end{cases} \tag{4}$$

Equation (4) relates the cost function to the discriminant function of the MAP decision rule, which is applied according to the parameter estimates in (2). Thus, up to additive or multiplicative constants, the criterion function turns out to be [16]

$$J(\tau) = \sum_{i=0}^{1} \hat{P}_{i\tau} (\ln \hat{\sigma}_{i\tau} - \ln \hat{P}_{i\tau}) \tag{5}$$

and the optimal threshold τ^* is defined as the "minimum-error threshold," i.e., $\tau^* = \arg \min \{J(\tau) : \tau = 0, 1, \ldots, Z - 1\}$.

B. Proposed Change-Detection Approach

Let $\mathcal{I}_0$ and $\mathcal{I}_1$ be the two equal-sized coregistered SAR amplitude images acquired over the same geographical area at times t_0 and t_1, respectively ($t_1 > t_0$). We model the image acquired at each date t_j as a set $\mathcal{I}_j = \{r_{j1}, r_{j2}, \ldots, r_{jN}\}$ (N being the number of pixels) of i.i.d. random variables[1] ($j = 0, 1$) [23]. The proposed method aims at detecting the changes that occurred in the area of interest during the time interval $[t_0, t_1]$.

In this context, the well-known multiplicative "speckle" noise model for SAR intensity data renders the classical image-differencing approach to change detection [13] not suitable for SAR imagery. On the contrary, image ratioing [1], [5], when applied to SAR intensity or amplitude images (or, equivalently, image differencing when applied to logarithmically transformed images), prevents undesired effects [1], [5], [24]. Consequently, the proposed method adopts the image-ratioing approach, i.e., it generates a ratio image $\mathcal{R} = \{u_1, u_2, \ldots, u_N\}$, where $u_k = r_{0k}/r_{1k}$ ($k = 1, 2, \ldots, N$). Denoting by H_0 and H_1 the no-change and change hypotheses, respectively, a thresholding decision rule can be applied to $\mathcal{R}$ to distinguish quantitatively between H_0 and H_1 [1].

To detect the changes corresponding both to a backscatter coefficient increase and to a backscatter coefficient decrease, a double-threshold approach could be used, i.e., the kth pixel could be labeled as no-change if $\tau_1 < u_k \leq \tau_2$ and as change if $u_k \leq \tau_1$ or $u_k > \tau_2$ ($k = 1, 2, \ldots, N$), where τ_1

---

[1]This approach is widely accepted in the context of estimation theory [22] and operatively corresponds to discarding, in the estimation process, the contextual information associated with the correlation among neighboring pixels in an image.

and τ_2 $(\tau_1 < 1 < \tau_2)$ are two thresholds to be selected jointly. However, to simplify the threshold-selection process, a single-threshold approach is typically adopted in the SAR change-detection literature [1], [14], i.e., the kth pixel is labeled as no-change if $u_k \leq \tau$ and as change if $u_k > \tau$ $(k = 1, 2, \ldots, N)$ [1], [14], where τ is a threshold to be set properly to minimize the number of misclassified pixels. Specifically, this decision rule aims at detecting the changes corresponding to a backscatter coefficient decrease in $[t_0, t_1]$ [1]. One can detect the changes corresponding to a backscatter coefficient increase by such a single-threshold approach, if one applies this procedure separately to the "reverse-direction" ratio image $\tilde{\mathcal{R}} = \{\tilde{u}_1, \tilde{u}_2, \ldots, \tilde{u}_N\}$, where $\tilde{u}_k = r_{1k}/r_{0k} = 1/u_k (k = 1, 2, \ldots, N)$.

In this paper, the single-threshold approach is adopted, and the problem of an automatic unsupervised selection of the threshold τ is addressed by extending to the context of SAR amplitude images the method that is proposed in [17] and [18] for change detection in optical imagery and that is based on K&I. A direct application of K&I to $\mathcal{R}$ is not feasible due to the considerable non-Gaussianity of SAR amplitude ratio data [1]. Hence, a generalization of K&I, which allows one to take into account non-Gaussian data as well, is proposed. In particular, as the pixel values $\{r_{jk}\}_{k=1}^N$ in each image $\mathcal{I}_j$ are assumed to be i.i.d. $(j = 0, 1)$, the amplitude ratios $\{u_k\}_{k=1}^N$ in $\mathcal{R}$ also turn out to be i.i.d. We assume a parametric model $p_i(\cdot|\theta_i)$ for the pdf of u_k $(k = 1, 2, \ldots, N)$ under H_i, where $\theta_i \in \mathbb{R}^{\ell_i}$ is the parameter vector of the distribution $(i = 0, 1)$. Assuming that the ratio image $\mathcal{R}$ is to be quantized into Z gray levels $\{0, 1, \ldots, Z-1\}$ with (normalized) histogram $\{h(u) : u = 0, 1, \ldots, Z-1\}$, K&I is generalized by defining, for each value $\tau \in \{0, 1, \ldots, Z-1\}$ of the threshold, the following cost function $c(u, \tau)$:

$$c(u, \tau) = \begin{cases} -\ln \hat{P}_{0\tau} - \ln p_0(u|\hat{\theta}_{0\tau}), & \text{for } u \in R_{0\tau} \\ -\ln \hat{P}_{1\tau} - \ln p_1(u|\hat{\theta}_{1\tau}), & \text{for } u \in R_{1\tau} \end{cases} \quad (6)$$

where $R_{i\tau}$ is defined as in (3), $\hat{P}_{i\tau}$ is computed as in (2), and $\hat{\theta}_{i\tau}$ is an estimate of the parameter vector θ_i that is computed according to the gray levels in $R_{i\tau}$ $(i = 0, 1)$. Plugging (6) into (1) yields, after some algebraic manipulations, the following generalized criterion function:

$$J(\tau) = -\sum_{i=0}^{1} \left[\hat{P}_{i\tau} \ln \hat{P}_{i\tau} + \sum_{u \in R_{i\tau}} h(u) \ln p_i(u|\hat{\theta}_{i\tau}) \right] \quad (7)$$

whose minimization yields the optimal threshold.

The application of this generalized Kittler and Illingworth thresholding algorithm (GKIT) requires the preliminary definitions of a suitable conditional parametric model $p_i(\cdot|\theta_i)$ for each hypothesis H_i and of the corresponding parameter-estimation strategy to compute $\hat{\theta}_{i\tau}$ according to the gray levels in $R_{i\tau}$ $(i = 0, 1)$. Toward this end, three different parametric pdfs are proposed here to model the ratio image (each one to be used according to the specific parameter-estimation strategies): They are based on the usual Nakagami-Gamma, Weibull, and log-normal models for the SAR amplitude images $\mathcal{I}_0$ and $\mathcal{I}_1$, respectively, and are described in Sections II-C–E.

C. Nakagami-Ratio GKIT

The first proposed version of GKIT operates in the context of the well-known Nakagami model for SAR amplitude data (corresponding to the Gamma model for the intensity data [1], [20]). This model represents the standard parametric pdf for the pixel intensity in the nontextured areas of a SAR multilook image [1]. Specifically, under each hypothesis H_i, assuming the SAR images acquired at t_0 and t_1 present a zero complex correlation between each other [1], [25] and to have the same equivalent number of looks (ENL), the following parametric model holds for the amplitude ratio pdf (see Appendix A):

$$p_i(u|L_i, \gamma_i) = \frac{2\Gamma(2L_i)}{\Gamma^2(L_i)} \frac{\gamma_i^{L_i} u^{2L_i-1}}{(\gamma_i + u^2)^{2L_i}}, \qquad u > 0 \quad (8)$$

where L_i and γ_i $(L_i, \gamma_i > 0)$ are the distribution parameters $(i = 0, 1)$, and $\Gamma(\cdot)$ is the usual Gamma function [26]. It is worth noting that, according to the temporal correlation between the images acquired over the same area, the aforementioned conditional uncorrelation assumption may turn out to be unrealistic. However, this assumption is often accepted as an approximation in the SAR change-detection literature [1], [5] to avoid dealing with more cumbersome conditional parametric models and, hence, with more complicated parameter-estimation procedures. The same comment holds with regard to the assumption of equal ENL values at the two dates.

As detailed in Appendix A, a feasible estimation technique for the parametric model in (8) (hereafter denoted simply by the Nakagami ratio) is the MoLC, which is a recently proposed parameter-estimation methodology based on the generalization of the concepts of characteristic function and moment-generating function [23] by using Mellin transforms [27] instead of the usual Fourier and Laplace transforms [19], [20], [28]. Specifically, MoLC exploits the Mellin transform theory to state a set of equations relating the unknown parameters to logarithmic moments or logarithmic cumulants ("log-cumulants" for short) of the gray-level distribution [20], thus expressing the parameter-estimation problem as the solution of a set of (typically nonlinear) equations. The method has been specifically developed in the context of SAR-oriented parametric models and has been proven to be numerically feasible and fast for many SAR-specific models (e.g., the Gamma, Nakagami, K, Weibull, and log-normal distributions [29], the symmetric-α-stable generalized Rayleigh model [29], [30], and the generalized Gaussian–Rayleigh model [19]) and to exhibit good theoretical estimation properties [19], [29].

We propose here to adopt MoLC to estimate the parameters of the Nakagami-ratio distribution of (8) due to the aforementioned good theoretical properties of this estimation method and to the simplicity of the resulting nonlinear equations. Specifically, in Appendix A, we prove that MoLC provides for the Nakagami ratio the following equations:

$$2\kappa_{1i} = \ln \gamma_i \qquad 2\kappa_{2i} = \Psi(1, L_i) \quad (9)$$

where $\kappa_{1i} = E\{\ln u|H_i\}$ and $\kappa_{2i} = \text{Var}\{\ln u|H_i\}$ are the first- and second-order log-cumulants, respectively $(i = 0, 1$ $\text{Var}\{\cdot\}$ denotes the variance operator), and $\Psi(1, \cdot)$ is the first-order polygamma function (i.e., the second logarithmic derivative of the Gamma function [20], [27]). Specifically, the

estimates $\hat{\kappa}_{1i\tau}$ and $\hat{\kappa}_{2i\tau}$ of κ_{1i} and κ_{2i} can be computed according to the histogram of the ratio image $\mathcal{R}$ as follows:

$$\hat{\kappa}_{1i\tau} = \frac{\sum_{u \in R_{i\tau}} h(u) \ln u}{\sum_{u \in R_{i\tau}} h(u)} \quad \hat{\kappa}_{2i\tau} = \frac{\sum_{u \in R_{i\tau}} h(u)(\ln u - \hat{\kappa}_{1i\tau})^2}{\sum_{u \in R_{i\tau}} h(u)} \tag{10}$$

and the estimates $\hat{L}_{i\tau}$ and $\hat{\gamma}_{i\tau}$ of L_i and γ_i can be derived by solving (9). In particular, $\hat{\gamma}_{i\tau}$ is computed analytically, and due to the continuity and strict monotonicity of the polygamma function $\Psi(1, \cdot)$, the numerical computation of $\hat{L}_{i\tau}$ does not involve critical numerical issues and can be performed by using the simple bisection method [31]. In the following, the resulting Nakagami-ratio GKIT algorithm will be denoted by NR-GKIT. Note that, in the K&I context, the estimation of the parameters of each Gaussian conditional distribution involves only the first two moments. A similar property holds also for the non-Gaussian NR-GKIT approach: The first two logarithmic moments of each conditional distribution are sufficient to estimate the distribution itself because the pdf in (8) depends on just two parameters, namely γ_i and L_i, and the related MoLC equations admit a unique solution (γ_i^*, L_i^*) for each couple $(\kappa_{1i}, \kappa_{2i})$ $[i = 0, 1;$ see (9)].

D. Log-Normal GKIT

The second proposed version of GKIT assumes the amplitude data in the image $\mathcal{I}_j$ acquired at each date t_j and conditioned to each hypothesis H_i ($i = 0, 1$ and $j = 0, 1$) to be distributed according to a log-normal model, which is frequently accepted as a heuristic parametric pdf for SAR intensity and amplitude distributions [1], [30]. Under each hypothesis H_i ($i = 0, 1$), if the pixel value r_{jk} of the kth pixel in $\mathcal{I}_j$ is log-normally distributed, its logarithm $\ln r_{jk}$ has a Gaussian distribution ($j = 0, 1$), which yields a Gaussian model also for the log-ratio $\ln u_k = \ln r_{0k} - \ln r_{1k}$ and, consequently, a log-normal model for the ratio u_k ($i = 0, 1$; $k = 1, 2, \ldots, N$), i.e.,

$$p_i(u|\kappa_{1i}, \kappa_{2i}) = \frac{1}{u\sqrt{2\pi\kappa_{2i}}} \exp\left[-\frac{(\ln u - \kappa_{1i})^2}{2\kappa_{2i}}\right], \quad u > 0 \tag{11}$$

where κ_{1i} and κ_{2i} are again the first- and second-order log-cumulants. Thus, in this case, the MoLC-based parameter-estimation task turns out to be very simple, as the distribution parameters are directly the first- and second-order log-cumulants [29]; then, they can be estimated by using (10). Plugging these estimates into (7) yields (up to additive and multiplicative constants) the following expression for the log-normal GKIT criterion function:

$$J(\tau) = \sum_{i=0}^{1} \hat{P}_{i\tau}\left(\frac{1}{2}\ln\hat{\kappa}_{2i\tau} - \ln\hat{P}_{i\tau}\right). \tag{12}$$

It is worth noting that this criterion function formulation turns out to be very similar to the standard K&I [see (5)], which is an expected result, as the current log-normal conditional model can be related to the Gaussian conditional one adopted by the standard K&I simply by transforming the gray levels according to a logarithmic mapping. In the following, the resulting log-normal GKIT algorithm will be simply denoted by LN-GKIT.

E. Weibull-Ratio GKIT

In the third proposed version of GKIT, we assume that the amplitudes at the two acquisition dates are independent and Weibull-distributed with the same values for the shape parameters. Therefore, we propose the following ratio amplitude H_i-conditional pdf ($i = 0, 1$):

$$p_i(u|\eta_i, \lambda_i) = \eta_i \lambda_i^{\eta_i} \frac{u^{\eta_i - 1}}{(\lambda_i^{\eta_i} + u^{\eta_i})^2}, \quad u > 0 \tag{13}$$

where η_i and λ_i ($\eta_i, \lambda_i > 0$) are the distribution parameters (in the following, this parametric family will be named Weibull ratio; its analytical derivation is reported in Appendix B). As remarked for the zero-complex-correlation assumption stated with regard to NR-GKIT, the aforementioned independence assumption between the gray levels at different dates is also accepted as a simplifying hypothesis, which discards the temporal contextual information associated with the couple $(\mathcal{I}_0, \mathcal{I}_1)$ of images. The assumption of equal values for the shape parameters at different dates plays the role of a simplifying hypothesis as well.

Furthermore, for the Weibull-ratio distribution, we propose to adopt MoLC as a parameter-estimation strategy. The following relations between the distribution parameters and the first- and second-order conditional log-cumulants κ_{1i} and κ_{2i} ($i = 0, 1$) are proven in Appendix B:

$$\kappa_{1i} = \ln \lambda_i \quad \kappa_{2i} = \frac{2\Psi(1,1)}{\eta_i^2}. \tag{14}$$

Hence, for each threshold value $\tau \in \{0, 1, \ldots, Z-1\}$, the histogram-based estimates $\hat{\kappa}_{1i\tau}$ and $\hat{\kappa}_{2i\tau}$ are computed according to (10), and the estimates $\hat{\eta}_{i\tau}$ and $\hat{\lambda}_{i\tau}$ are obtained by solving (14) ($i = 0, 1$). This solution process is carried out analytically for both $\hat{\eta}_{i\tau}$ and $\hat{\lambda}_{i\tau}$. The resulting algorithm will be denoted by the Weibull-ratio GKIT (WR-GKIT). The same remarks made in Section II-C on the sufficiency of just two parameters for the estimation of a Nakagami-ratio pdf hold also for a Weibull-ratio distribution.

III. EXPERIMENTAL RESULTS

A. Data Sets for Experiments

The proposed GKIT algorithm (in its three versions) was tested on two real multitemporal SAR data sets made up of two 700×280 pixel-sized images each, which are acquired over an agricultural area near Pavia, Italy, on April 16, 1994 and April 18, 1994, respectively. The first data set, which consists of two four-look SIR-C images (C-band, HH polarization), will be denoted synthetically by "Pavia-C," whereas the second data set, which consists of two four-look XSAR images (X-band, VV polarization), will be identified by "Pavia-X" [see Fig. 1(a) and (b)]. Data sets acquired by distinct sensors, with different acquisition frequencies and polarizations, have been chosen to assess the capability of the proposed approach to adapt to different types of input SAR data.

Ground changes occurred in the scene, as several rice fields were flooded between the two acquisition dates. In particular, a test map [Fig. 1(c)], which presents 11 287 no-change test
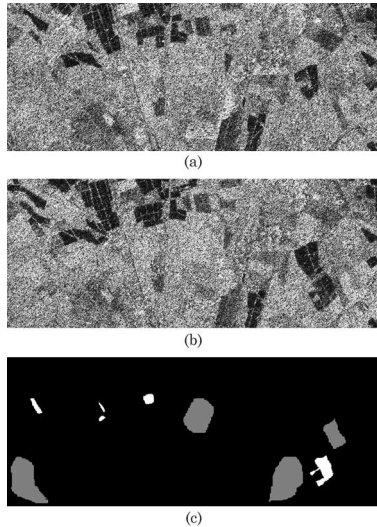
Fig. 1. Pavia-X data set for experiments: (a) April 16 image and (b) April 18 image after histogram equalization and (c) test map. Color legend for (c): white, change; gray, no-change; black, unlabeled pixels.

TABLE I
EQUIVALENT ENLS FOR THE IMAGES USED IN THE EXPERIMENTS (IN BOTH THE NONFILTERED AND SPECKLE-FILTERED VERSIONS)

Filtering iterations	Acquisition Date	"Pavia-X"	"Pavia-C"
none	April 16	3.19	3.65
	April 18	3.13	3.58
1	April 16	40.02	27.10
	April 18	39.65	26.84
2	April 16	63.45	47.17
	April 18	57.75	56.08

pixels and 1870 change test pixels, was available. The ENLs of the adopted images (computed over homogeneous regions as described in [1]) are reported in Table I. Such ENLs are quite low (always below 4), which suggests quite a strong presence of speckle in the considered data.

B. Experiment I

During the first experiment, the behavior of the proposed technique was analyzed by applying GKIT to the samples (quantized over $Z = 256$ gray levels) of the ratio image obtained by ratioing the April 16 image by the April 18 one (for both Pavia-X and Pavia-C) and by focusing only on the pixels within the test regions. Table II reports the detection accuracy (i.e., the percentage of change test pixels correctly labeled as such), the false alarm rate (i.e., the percentage of no-change test pixels erroneously detected as change), and the (overall) error rate (i.e., the percentage of erroneously labeled test pixels). Focusing only on the test samples allows one to compare the GKIT results with the ones that could be obtained by searching exhaustively the threshold value that yields the change map with the lowest error rate on the adopted test set (in the following, this reference threshold-selection approach will be named "test-optimal"; see Table II). In particular, the search range [0,255] was chosen with a discretization step that is equal to 0.02. This optimal result is achieved by knowing in advance the correct change/no-change labels of the test samples.

TABLE II
EXPERIMENT I: CHANGE-DETECTION PERFORMANCES PROVIDED BY GKIT AND BY TEST-OPTIMAL APPLIED TO THE EMPLOYED DATA SETS IN THEIR ORIGINAL VERSIONS (i.e., WITHOUT SPECKLE FILTERING)

Thresholding	"Pavia-X"				"Pavia-C"			
	Error rate	Detection accuracy	False-alarm rate	τ^*	Error rate	Detection accuracy	False-alarm rate	τ^*
LN-GKIT	14.21%	0%	0%	255	4.16%	77.22%	1.07%	12
NR-GKIT	14.21%	0%	0%	255	4.52%	72.51%	0.72%	14
WR-GKIT	14.21%	0%	0%	255	5.73%	61.66%	0.33%	18
Test-optimal	14.21%	0%	0%	255	4.10%	79.52%	1.39%	11.3

As shown in Table II, a direct application of GKIT to the original SAR images was poorly effective due to the strong presence of speckle that yielded a very large overlap between the change and no-change hypotheses in the (one-dimensional) feature space. In particular, the best result obtained on Pavia-C is given by LN-GKIT and is characterized by a good error-rate value (namely 4.16%) in spite of a quite low detection-accuracy value (77.22%). In this case, NR-GKIT and WR-GKIT provided even worse results. On the other hand, poor results were obtained on Pavia-X, as the three GKIT versions did not identify the change regions at all, i.e., the corresponding criterion functions were monotonically decreasing in [0,255] (no internal minima). In particular, the histogram of the ratio image turned out to be monomodal due to the heavy tail of the no-change distribution (caused by speckle) and to the fact that the prior probability of no-change is much higher than the one of change. Consequently, the mode related to change is completely lost inside the tail of the no-change mode. In this case, the resulting overall error rate was equal to the relative frequency of change in the test set (i.e., $1870/(1870 + 11287) = 14.21\%$). More generally, we note that the overall error rates intrinsically depend on the numbers of test samples for the two hypotheses, i.e., they are affected by the specific choice of the test data set. On the other hand, the difficulty in effectively separating change from no-change in the amplitude ratio feature space is confirmed by test-optimal, as this approach achieved a change-detection result that is very similar to the LN-GKIT one on Pavia-C (in particular, the difference between the test-optimal threshold and the LN-GKIT one was only 0.7) and detected no change at all in Pavia-X (like GKIT).

Thus, a preliminary despeckling phase was performed by using the adaptive Gamma–MAP filter [1]. Gamma–MAP was chosen for its simplicity and because it is known from the literature to allow a good tradeoff between the quality of the filtered image and the execution time [1]. Gamma–MAP exploits a moving window of fixed width w to perform a local MAP estimation of the unknown backscatter coefficient according to Gamma models for the involved conditional and prior distributions [1]. One or more run(s) of the filter can be performed to achieve a good tradeoff between removing speckle and avoiding an oversmoothing of the image; w can also be tuned for this goal. In the present experiments, one or two iteration(s) of a 7×7 Gamma–MAP procedure was/were performed to test the effectiveness of the proposed change-detection method under different noise conditions. Both w and the number of iterations h were chosen by a trial-and-error procedure, as is usual in the context of SAR data classification. Here, we focused on

TABLE III
EXPERIMENT I: CHANGE-DETECTION PERFORMANCES PROVIDED BY
GKIT AND BY THE REFERENCE TEST-OPTIMAL THRESHOLDING
APPROACH, WHICH IS APPLIED TO PAVIA-X AFTER
7×7 GAMMA–MAP FILTERING

Filtering iterations	Thresholding	Error rate	Detection accuracy	False-alarm rate	τ^*
1	LN-GKIT	2.33%	95.72%	2.01%	6
	NR-GKIT	2.33%	95.72%	2.01%	6
	WR-GKIT	2.33%	95.72%	2.01%	6
	Test-optimal	1.53%	92.73%	0.58%	6.6
2	LN-GKIT	0.50%	99.36%	0.48%	9
	NR-GKIT	0.50%	99.36%	0.48%	9
	WR-GKIT	0.35%	97.54%	0.00%	10
	Test-optimal	0.18%	98.82%	0.02%	9.52

TABLE IV
EXPERIMENT I: CHANGE-DETECTION PERFORMANCES PROVIDED BY
GKIT AND BY THE REFERENCE TEST-OPTIMAL THRESHOLDING
APPROACH, WHICH IS APPLIED TO PAVIA-C AFTER
7×7 GAMMA–MAP FILTERING

Filtering iterations	Thresholding	Error rate	Detection accuracy	False-alarm rate	τ^*
1	LN-GKIT	1.65%	96.47%	1.34%	7
	NR-GKIT	2.10%	91.34%	1.01%	8
	WR-GKIT	2.10%	91.34%	1.01%	8
	Test-optimal	1.63%	96.31%	1.29%	7.14
2	LN-GKIT	1.12%	98.45%	1.05%	6
	NR-GKIT	1.12%	98.45%	1.05%	6
	WR-GKIT	1.09%	96.95%	0.77%	7
	Test-optimal	1.09%	96.95%	0.77%	7.02

the complete automatization of the threshold-selection process, whereas we did not address the problem of the automatic selection of the optimal value for h or w.

A sharp increase in ENL was obtained when switching from the original data to the despeckled image, even with just one Gamma–MAP iteration; a further significant speckle reduction resulted from the second iteration, which gave large ENL values (see Table I). As expected, this increase in ENL corresponded to a significant reduction in the impact of speckle on the detection results, as GKIT yielded good change-detection accuracies for both filtered versions of the data set, at error rates always lower than 2.5% (Tables III and IV). By focusing first on Pavia-X, the three GKIT versions provided the same threshold value in the case of one filtering iteration. In the case of two filtering iterations, LN-GKIT and NR-GKIT generated the same change map, whereas WR-GKIT gave a slightly better result. As far as Pavia-C, LN-GKIT provided the lowest error rate in the case of one filtering iteration, whereas WR-GKIT gave the best result in the case of two iterations, although the performances of the three GKIT versions were very close to one another. In all the cases, the threshold values automatically selected by GKIT were very close to the test-optimal ones (with a difference of approximately 1 or less). It is worth noting that the histogram-based threshold-selection approach adopted by GKIT (and by K&I) searches for an integer threshold, whereas the test-optimal strategy also considered noninteger values (with a discretization
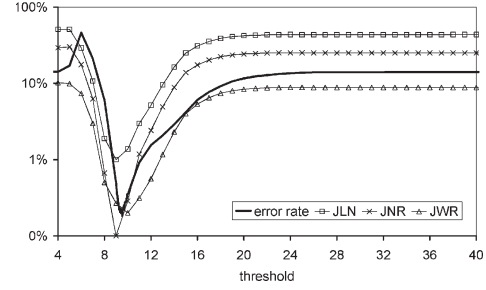

Fig. 2. Experiment I: logarithmic plot of the NR-GKIT, LN-GKIT, and WR-GKIT criterion functions $J_{\mathrm{NR}}(\cdot)$, $J_{\mathrm{LN}}(\cdot)$, and $J_{\mathrm{WR}}(\cdot)$ (up to a linear rescale) and of the error rate, versus the threshold value, in the case of Pavia-X with two Gamma–MAP iterations.

step that is equal to 0.02). However, taking into account such noninteger values would be possible in the GKIT framework as well by quantizing the ratio image on a scale presenting a (suitable) higher number of levels. For instance, the application of GKIT with a step that is equal to 0.02 can be simply accomplished by quantizing the ratio data over $256/0.02 = 13056$ levels. Furthermore, in this case, the proposed three versions of GKIT selected optimal thresholds that are very close to one another. In particular, the differences between the error rates obtained by steps 1 and 0.02 were always below 0.7%.

Good results were obtained on filtered images, although the development of the three pdf models adopted by GKIT does not take into account the filtering effect. When focusing, for instance, on NR-GKIT, the original amplitude is assumed to be conditionally Nakagami-distributed, but the gray levels in the Gamma–MAP filtered image are not expected to rigorously follow a Nakagami pdf. However, NR-GKIT turned out to be effective for such a speckle-filtered image, and this suggests a low sensitivity to deviations from the theoretical model. Similar remarks also hold for LN-GKIT and NR-GKIT.[2]

The similarity between the performances of the unsupervised GKIT approach and the test-optimal reference is further confirmed by an analysis of the behavior of the GKIT criterion functions. For instance, Fig. 2 plots such functions for Pavia-X (with two Gamma–MAP iterations) together with the overall error rate obtained by applying the threshold τ to the ratio image and by making use of the knowledge about the correct classification of the test pixels (as in test-optimal). A similar behavior can be noted for the three criterion functions, where each curve presents a single well-defined global minimum. In addition, a significant similarity can also be noted between such curves and the behavior of the error rate as a function of τ, which suggests that the unsupervised GKIT criterion function can be a good unsupervised indicator of the overall accuracy of the change map.

For the sake of comparison, the results of GKIT were compared with the ones of the automatic method recently proposed in [21], which addresses the SAR change-detection

---

[2]In particular, the Nakagami-ratio distribution is obtained from the theoretical Nakagami-Gamma model for multilook SAR intensity and amplitude, whereas the Weibull-ratio and log-normal pdfs are derived from the heuristic Weibull and log-normal models. The good change-detection results granted by all three pdfs in the case of speckle-filtered data suggest that they can represent effective heuristic models also after filtering. A more detailed analysis has been carried out and reported in Section III-D for the confirmation of this indirect deduction.

TABLE V
EXPERIMENT I: CHANGE-DETECTION PERFORMANCES PROVIDED
BY THE GGLR-GKIT METHOD PROPOSED IN [21]

Filtering iterations	"Pavia-X"			"Pavia-C"		
	Error rate	Detection accuracy	False-alarm rate	Error rate	Detection accuracy	False-alarm rate
none	14.92%	0.05%	0.83%	4.53%	72.51%	0.73%
1	3.61%	97.06%	3.72%	1.64%	96.47%	1.33%
2	0.23%	98.98%	0.10%	2.33%	99.04%	2.56%

TABLE VI
EXPERIMENT II: CHANGE-DETECTION PERFORMANCES PROVIDED
BY THE THREE VERSIONS OF GKIT AND BY THE GG LOG-RATIO
METHOD PROPOSED IN [21] (GGLR-GKIT)

Filtering iterations	Thresholding	"Pavia-X"			"Pavia-C"		
		Error rate	Detection accuracy	False-alarm rate	Error rate	Detection accuracy	False-alarm rate
none	LN-GKIT	14.62%	0.05%	0%	6.92%	52.14%	0.14%
	NR-GKIT	16.63%	46.63%	10.54%	10.58%	25.67%	0.02%
	WR-GKIT	14.21%	0%	0%	11.83%	16.79%	0%
	GGLR-GKIT	13.98%	5.78%	0.69%	6.02%	59.30%	0.27%
1	LN-GKIT	2.90%	80.37%	0.12%	2.64%	85.56%	0.68%
	NR-GKIT	2.90%	80.37%	0.12%	2.98%	81.71%	0.44%
	WR-GKIT	4.33%	69.84%	0.05%	3.55%	77.06%	0.34%
	GGLR-GKIT	9.52%	33.21%	0.03%	4.55%	69.14%	0.19%
2	LN-GKIT	0.92%	93.53%	0%	1.57%	92.57%	0.59%
	NR-GKIT	0.92%	93.53%	0%	2.00%	88.93%	0.50%
	WR-GKIT	0.92%	93.53%	0%	2.00%	88.93%	0.50%
	GGLR-GKIT	1.15%	91.93%	0%	4.51%	69.14%	0.14%

problem by generating a log-ratio image from the two SAR images $\mathcal{I}_0$ and $\mathcal{I}_1$ (i.e., it computes pixel-by-pixel the logarithm of the amplitude ratio) and by distinguishing change from no-change through the application of K&I to the log-ratio histogram. Specifically, a GG model [32] is postulated for the log-ratio pdfs conditioned to change and no-change and integrated in [21] into the K&I framework. Because this approach is a generalization of K&I, we shall denote it synthetically by GG log-ratio GKIT (GGLR-GKIT). It is worth noting that the algorithm proposed in [21] also includes a procedure to select automatically a suitable number of filtering iterations. This procedure has not been adopted in the present experiments to test both GGLR-GKIT and the proposed NR-GKIT, LN-GKIT, and WR-GKIT methods on the same prefiltered images, thus focusing on the two distinct threshold-selection procedures. The results of the application of this method to Pavia-C and Pavia-X are shown in Table V.

Overall, the GGLR-GKIT technique gave results similar to the ones obtained by the proposed methods. In particular, it yielded slightly better performances than our GKIT when applied to Pavia-X with two filtering iterations and to Pavia-C with one iteration (although with error rate differences below 0.15%), whereas the proposed techniques gave more accurate results on Pavia-X with one iteration and on Pavia-C with two iterations (with error rate differences above 1.2%). A small increase in the overall error rate (+0.69%) was exhibited by GGLR-GKIT when switching from one to two filtering iterations, which correspond to an improvement in the detection accuracy (+2.57%) and an increase in the false alarm rate (+1.23%). This suggests that the optimal number of filtering iterations for such a technique may be one (when using more than two iterations, a further increase in the error rate was observed).

C. Experiment II

During the second experiment, GKIT was applied to Pavia-X and Pavia-C by considering all the image pixels (Table VI). Compared with experiment I, in this case, a more realistic operational context is employed, as an unsupervised change-detection task typically involves the analysis of the whole image area, without the restriction to a (test) sample subset. In this case, a comparison with a test-optimal strategy is not feasible due to the lack of information about the true change/no-change labels of all the image pixels. The test set has been used, in any case, to evaluate the obtained accuracies.

Without speckle reduction, a poor result was obtained in this case as well (see Table VI). On the other hand, very good results were achieved on prefiltered images (with error rates
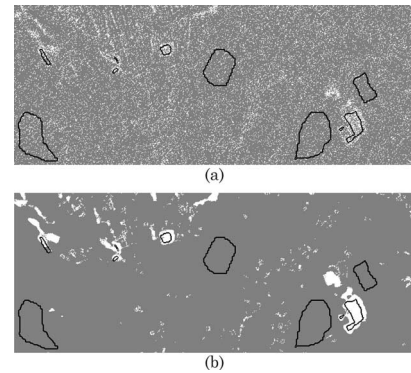

Fig. 3. Experiment II. Change maps obtained by NR-GKIT on Pavia-X, in the cases of (a) nonfiltered input images and (b) filtered images with two 7×7 Gamma–MAP iterations. Color legend: white, change; gray, no-change [as a reference, the black lines mark the borders of the test fields of the test map in Fig. 1(c)].

always lower than 5%), and a significant accuracy increase was observed when performing a more effective speckle reduction (i.e., when switching from one to two Gamma–MAP iterations). Focusing, for instance, on Pavia-X and on NR-GKIT, the change map obtained without speckle filtering [Fig. 3(a)] turned out to be very noisy due to the strong impact of speckle on the classification results. However, an effective two-iteration speckle reduction allowed to obtain the change map shown in Fig. 3(b), which exhibited a very good detection accuracy (93.53%) with no false alarm pixels over the whole test set, although some false alarms due to the residual noise can be noted in other image areas. Some examples of the remaining missed alarms are given in Fig. 4. As can be noticed by a visual inspection, the ground changes that occurred in the circled area in Fig. 4(b) yield a backscatter coefficient variation of lower intensity, as compared with the other changes in the image [see Figs. 1(b) and 4(b)]; thus, they turn out to be partially mistaken for no-change pixels.

The GGLR-GKIT technique was slightly more effective than the proposed three procedures when applied to both Pavia-C and Pavia-X without speckle reduction, although still yielding
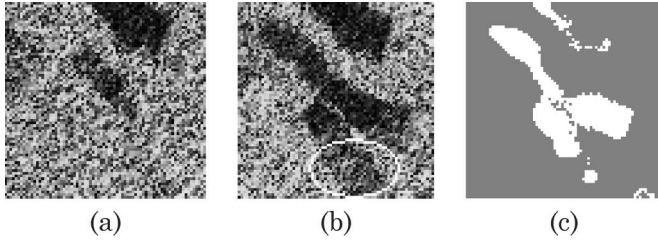
Fig. 4. Experiment II. Details of (a) the April 16 image and (b) April 18 image of the Pavia-X data set and (c) the change map obtained by NR-GKIT for Pavia-X in the case of two 7 × 7 Gamma–MAP iterations. The color legend is the same as in Fig. 3. The white circle in (b) highlights a missed alarm area.

TABLE VII
CORRELATION COEFFICIENTS BETWEEN THE AMPLITUDE RATIO HISTOGRAMS OF THE CHANGE AND NO-CHANGE TEST AREAS AND THE ESTIMATED LOG-NORMAL (LN), NAKAGAMI-RATIO (NR), AND WEIBULL-RATIO (WR) PDFs (GENERATED BY THE APPLICATIONS OF LN-GKIT, NR-GKIT, AND WR-GKIT, RESPECTIVELY, TO THE TEST DATA)

Filtering iterations	Parametric model	"Pavia-X"		"Pavia-C"	
		"no-change"	"change"	"no-change"	"change"
none	LN	not defined	not defined	98.54%	70.24%
	NR	not defined	not defined	97.79%	83.17%
	WR	not defined	not defined	97.38%	67.22%
1	LN	99.96%	98.13%	99.57%	86.77%
	NR	99.98%	99.27%	99.68%	92.11%
	WR	99.94%	99.62%	99.91%	91.60%
2	LN	99.71%	97.47%	99.90%	91.57%
	NR	99.69%	95.37%	99.94%	89.02%
	WR	98.78%	98.26%	99.96%	91.66%

low detection accuracies (namely 59.30% and 5.78%). It provided good change-detection results, with error rates lower than 10%, when also applied to the filtered versions of Pavia-X and Pavia-C. However, Table VI suggests a globally higher effectiveness for the proposed techniques, which allowed achieving (at least on the two considered data sets) lower error rates with higher detection accuracies for all the filtered images (especially in the cases of Pavia-X with one Gamma–MAP iteration and of Pavia-C with two iterations).

D. PDF Estimation Issues

GKIT, like K&I, implicitly generates unsupervised estimates of the conditional pdfs. To focus on the quality of such estimates, we give in Table VII the correlation coefficients between the histograms of the change and no-change test areas in the ratio images and the corresponding pdf estimates (to allow a fair comparison, such results refer again to the setting of experiment I; see Section III-B). Indeed, the GKIT estimates are not defined in the case of the nonfiltered Pavia-X data set because GKIT selected 255 as a threshold value. Very high correlation coefficients (always above 95% and often above 99%) were obtained by all three versions of GKIT for both change and no-change in Pavia-X and for no-change in Pavia-C. A visual comparison between the histograms and the pdf estimates confirms such conclusions (see Fig. 5).
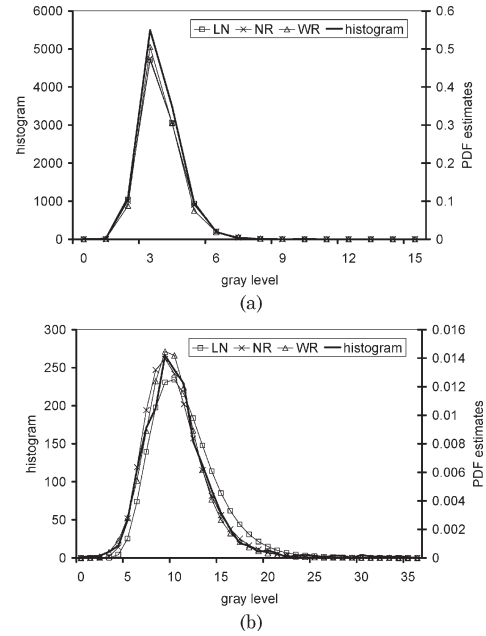

Fig. 5. Pavia-X (one Gamma–MAP iteration). Plots of the amplitude ratio histograms of the (a) no-change test area and (b) change test area, together with the estimated log-normal (LN), Nakagami-ratio (NR), and Weibull-ratio (WR) pdfs (generated by the applications of LN-GKIT, NR-GKIT, and WR-GKIT, respectively, to the test data).
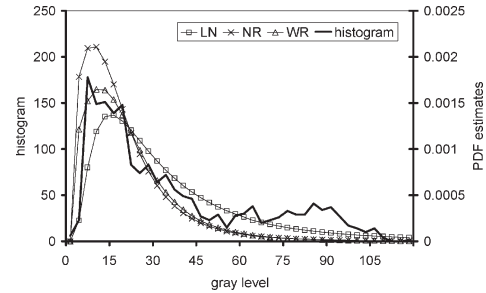

Fig. 6. Pavia-C (two Gamma–MAP iterations). Plots of the amplitude ratio histogram of the change test areas, together with the estimated log-normal (LN), Nakagami-ratio (NR), and Weibull-ratio (WR) pdfs (generated by the applications of LN-GKIT, NR-GKIT, and WR-GKIT, respectively, to the test data).

Significantly lower correlation coefficients were obtained for change in Pavia-C. This worse result was due to the fact that the corresponding histogram was bimodal (Fig. 6), whereas the log-normal, Nakagami-ratio, and Weibull-ratio pdfs were intrinsically monomodal. Such bimodality was probably to be ascribed to the presence of distinct changed areas with different intensities of the variations in the backscatter coefficient. However, also for this data set, good change-detection performances were obtained (see Section III-B), which seem to confirm the robustness of the proposed change-detection method to deviations from the postulated theoretical model.

Focusing on the monomodal distributions, Table VII confirms the similar behaviors of the three GKIT versions also in terms of pdf estimation. In particular, a very good fit of the histograms to the estimated pdfs was obtained also for speckle-filtered images. This further confirms the effectiveness of the log-normal, Nakagami-ratio, and Weibull-ratio distributions (endowed with MoLC) as heuristic models for the statistics of

the ratios of the SAR amplitudes after despeckling (at least with regard to the adopted Gamma–MAP filter).

IV. CONCLUSION

The numerical results of the experiments on SAR images suggest that the accuracy of the proposed approach is affected by the presence of speckle. In particular, the detection accuracy turns out to suffer from the strong overlapping of the change and no-change pdfs that consequently occurs. On the contrary, the proposed method proves to be effective when applied to speckle-filtered images, with similar performances for the three versions of the technique. In particular, a comparison between the results of the developed unsupervised algorithm and the results of a test-optimal strategy (i.e., an exhaustive search for the threshold value achieving the lowest possible error rate over the employed test set) further confirmed the effectiveness of the method, as the achieved accuracy is only slightly better than the one granted by our method. The flexibility of the GKIT technique is further confirmed by the fact that good results were obtained on images acquired by two distinct sensors (i.e., XSAR and SIR-C) with different bands and polarizations.

The experiments did not point out a significant difference among the performances of the three proposed versions of GKIT, which obtained change-detection results very close to one another. This makes the choice of a specific parametric model not very critical. Anyway, to select a suitable ratio model (among the three models that have been considered) for a given application, an indication can be drawn from the fact that the three models derive from the corresponding SAR amplitude distributions. Such distributions are known from the SAR literature to describe correctly the statistics of several land-cover typologies [1], [28]. Given a specific change-detection application, a user could adopt the GKIT version whose pdf model best describes the land covers involved in the application.

The use of GKIT after speckle filtering produced accurate change maps, although the effect of despeckling on the distribution of the amplitude values was not considered in the theoretical development of the method. This result suggests that the adopted pdfs are quite good empirical models for the distributions of the filtered images as well, as it is confirmed by specific comparisons of the ratio data histograms with the pdf estimates generated by GKIT. For one of the data sets, the comparisons also pointed out the possible multimodality of the change hypothesis, which affects the pdf estimation accuracy.

More generally, when two typologies of change are present in the data set, one corresponding to an increase and the other to a decrease in the backscatter coefficient, two separate applications of GKIT to the two possible ratio images (see Section II-B) are required. Further experiments (not reported here for the sake of brevity) have confirmed the effectiveness of this two-stage procedure. On the other hand, if multiple changes are present in the same direction (i.e., several backscatter coefficient increases or several backscatter coefficient decreases) and if the related histogram modes are sharply separated, GKIT may erroneously select a threshold value in the middle between two change modes, thus merging the no-change class with some of the change subclasses. However, this is an expected behavior because GKIT is based on the assumption of a monomodal distribution for each hypothesis. To overcome this problem,

a multithreshold extension of GKIT that is similar to the multithreshold extension of K&I proposed within the Gaussian framework [16] should be developed.

In the experimental comparison between GKIT and the recently proposed thresholding method for SAR change detection in [21], GKIT yielded slightly more accurate results. However, overall good results were generated by the method in [21] as well; furthermore, this method includes a procedure to optimize automatically the number of filtering iterations that was not utilized for the comparison. The integration of such a procedure into the proposed approach would be an interesting extension of the proposed method; however, a specific study would be needed because a simple application of this technique to our case did not give good results in some preliminary experiments.

GKIT implicitly integrates the processes of threshold selection and parametric estimation of the amplitude ratio pdfs conditioned to change and no-change. However, the resulting pdf estimates (as the Gaussian estimates generated by K&I) can be expected to be slightly biased, according to the specific parameter-estimation strategy adopted by K&I and by GKIT [16]. To remove this bias, a further parameter-estimation stage could be performed by adopting more sophisticated methods (e.g., [33]–[35]), which were initialized by the GKIT estimates. In particular, a possible development of the present research work will lie in the integration of the Nakagami-ratio, Weibull-ratio, and log-normal models in such estimation techniques to improve the parameter estimates provided by GKIT. The use of further parametric models for the change and the no-change hypotheses (e.g., based on the Fisher [20] or on the K [1] distributions) could be considered for future development. A further development of GKIT would be the integration of more general "minimum-risk" decision approaches to penalize differently false alarm and missed alarm errors [22].

When finally focusing on computational issues, it can be noted that all the three GKIT versions exhibit very short computation times, which are almost independent of the image size, because GKIT directly deals only with the image histogram. Hence, the image size only affects the time required to generate the histogram, but not the time needed to compute the optimal threshold.

APPENDIX A
NAKAGAMI-RATIO PARAMETRIC FAMILY

Let us introduce, in general, two Gamma-distributed SAR intensities v_0 and v_1 (corresponding to two Nakagami-distributed SAR amplitudes $r_0 = \sqrt{v_0}$ and $r_1 = \sqrt{v_1}$) with the same number of independent looks L and with means $\mu_0 = E\{v_0\}$ and $\mu_1 = E\{v_1\}$, respectively. Assuming a zero complex correlation between the corresponding SAR images, the pdf of the intensity ratio $q = v_0/v_1$ is given by [1]

$$p_q(q) = \gamma^L \frac{\Gamma(2L)}{\Gamma^2(L)} \frac{q^{L-1}}{(\gamma + q)^{2L}}, \qquad q > 0 \qquad (15)$$

where $\gamma = \mu_0/\mu_1$. This yields the following expression for the pdf of the amplitude ratio $u = r_0/r_1 = \sqrt{q}$ [23]:

$$p_u(u) = 2u p_q(u^2) = \gamma^L \frac{2\Gamma(2L)}{\Gamma^2(L)} \frac{u^{2L-1}}{(\gamma + u^2)^{2L}}, \qquad u > 0. \qquad (16)$$

As described in [29], the Mellin transform theory allows proving the following expressions for the logarithmic mean and variance (i.e., for the first- and second-order log-cumulants of a Gamma-distributed intensity:

$$E\{\ln v_j\} = \ln \mu_j + \Psi(L) - \ln L, \qquad j = 0, 1$$
$$\mathrm{Var}\{\ln v_j\} = \Psi(1, L), \qquad j = 0, 1 \quad (17)$$

where $\Psi(\cdot)$ is the digamma function (i.e., the first logarithmic derivative of the Gamma function [20], [27]). Because $2\ln u = \ln q = \ln v_0 - \ln v_1$, the logarithmic mean (i.e., the first-order log-cumulant) of the amplitude ratio u is given by

$$\kappa_1 = E\{\ln u\} = \frac{1}{2}(\ln \mu_0 - \ln \mu_1) = \frac{1}{2}\ln \gamma. \quad (18)$$

Similarly, the zero-complex-correlation assumption also yields a zero correlation between the two intensities (i.e., $E\{v_0 v_1\} = E\{v_0\}E\{v_1\}$) [1], [25], which allows deriving the following expression for the logarithmic variance (i.e., the second-order log-cumulant) of the ratio u:

$$\kappa_2 = \mathrm{Var}\{\ln u\} = \frac{1}{4}\mathrm{Var}\{\ln q\}$$
$$= \frac{1}{4}\left(\mathrm{Var}\{\ln v_0\} + \mathrm{Var}\{\ln v_1\}\right) = \frac{1}{2}\Psi(1, L). \quad (19)$$

Therefore, when focusing on the change-detection case and employing the notations introduced in Sections II-B and C, the application of (18) and (19) to the amplitude ratio conditional pdf (8) yields (9) for the first- and second-order log-cumulants, which are conditioned to each hypothesis H_i ($i = 0, 1$).

APPENDIX B
WEIBULL-RATIO PARAMETRIC FAMILY

By employing the same notations of Appendix A, we adopt the following Weibull distribution for the SAR amplitude r_j [1]:

$$f_j(r) = \frac{\eta}{\xi_j^\eta} r^{\eta-1} \exp\left[-\left(\frac{r}{\xi_j}\right)^\eta\right], \qquad r > 0; \quad j = 0, 1 \quad (20)$$

where ξ_0 and ξ_1 are the scaling parameters, and η is a shape parameter [1]. We note that the same value for the shape parameter is implicitly assumed at both dates. This is analogous to the assumption of equal values for the ENL L at both dates in the context of (15). Similarly, if further assuming r_0 and r_1 to be independent (see Section II-E), the pdf of the amplitude ratio $u = r_0/r_1$ is given by [23], [29]

$$p_u(u) = \int_0^{+\infty} r f_0(ur) f_1(r)\, dr, \qquad u > 0. \quad (21)$$

Plugging (20) into (21) yields

$$p_u(u) = \frac{\eta^2 u^{\eta-1}}{(\xi_0 \xi_1)^\eta} \int_0^{+\infty} r^{2\eta-1} \exp\left[-A(u)r^\eta\right] dr \quad (22)$$

where

$$A(u) = \frac{1}{\xi_1^\eta} + \frac{u^\eta}{\xi_0^\eta}.$$

Therefore, the change of variable $r \mapsto \rho = A(u)r^\eta$, after simple algebraic manipulations, gives

$$p_u(u) = \frac{\eta u^{\eta-1}}{(\xi_0 \xi_1)^\eta A(u)^2} \int_0^{+\infty} \rho \exp(-\rho) d\rho = \eta u^{\eta-1} \frac{(\xi_0 \xi_1)^\eta}{(\xi_0^\eta + \xi_1^\eta u^\eta)^2} \quad (23)$$

and, finally, by introducing the auxiliary parameter $\lambda = \xi_0/\xi_1$, we now have

$$p_u(u) = \eta \lambda^\eta \frac{u^{\eta-1}}{(\lambda^\eta + u^\eta)^2}. \quad (24)$$

It is worth noting that, like the pdf of the two Gamma-distributed intensities, this Weibull-ratio pdf also explicitly depends only on the ratio λ of the single-date scaling parameters ξ_0 and ξ_1 and not on their absolute values.

As proven in [29], the following expressions are obtained by using Mellin transforms for the first- and second-order log-cumulants of the Weibull distribution:

$$E\{\ln r_j\} = \ln \xi_j + \frac{\Psi(1)}{\eta} \quad \mathrm{Var}\{\ln r_j\} = \frac{\Psi(1, 1)}{\eta^2} \quad (25)$$

which allows computing the following expression for the first-order log-cumulant of the amplitude ratio:

$$\kappa_1 = E\{\ln u\} = E\{\ln r_0\} - E\{\ln r_1\} = \ln \xi_0 - \ln \xi_1 = \ln \lambda \quad (26)$$

and, according to the independence assumption, the following result for the second-order log-cumulant:

$$\kappa_2 = \mathrm{Var}\{\ln u\} = \mathrm{Var}\{\ln r_0\} + \mathrm{Var}\{\ln r_1\} = \frac{2\Psi(1, 1)}{\eta^2}. \quad (27)$$

As for the previous Nakagami-ratio case, when focusing on the change-detection problem, the choice of a Weibull-ratio model for the amplitude ratio pdf conditioned to each hypothesis H_i [see (13)] allows stating the expression (14) for the H_i-conditional first- and second-order log-cumulants ($i = 0, 1$), thus resulting in the WR-GKIT algorithm.

ACKNOWLEDGMENT

REFERENCES

[1] C. Oliver and S. Quegan, *Understanding Synthetic Aperture Radar Images*. Norwood, MA: Artech House, 1998.
[2] E. S. Kasischke, J. M. Melack, and M. C. Dobson, "The use of imaging radars for ecological applications—A review," *Remote Sens. Environ.*, vol. 59, no. 2, pp. 141–156, Feb. 1997.
[3] J. E. S. Fransson, F. Walter, K. Blennow, A. Gustavsson, and L. M. H. Ulander, "Detection of storm-damaged forested areas using airborne

CARABAS-II VHF SAR image data," *IEEE Trans. Geosci. Remote Sens.*, vol. 40, no. 10, pp. 2170–2175, Oct. 2002.

[4] F. Siegert and A. A. Hoffmann, "The 1998 forest fires in East Kalimantan (Indonesia): A quantitative evaluation using high resolution ERS-2 SAR images and NOAA AVHRR hotspot data," *Remote Sens. Environ.*, vol. 72, no. 1, pp. 64–67, Apr. 2000.

[5] E. J. M. Rignot and J. J. Van Zyl, "Change detection techniques for ERS-1 SAR data," *IEEE Trans. Geosci. Remote Sens.*, vol. 31, no. 4, pp. 896–906, Jul. 1993.

[6] R. G. White, "Change detection in SAR imagery," *Int. J. Remote Sens.*, vol. 12, no. 2, pp. 339–360, 1990.

[7] X. Li and A. G. Yeh, "Multitemporal SAR images for monitoring cultivation systems using case-based reasoning," *Remote Sens. Environ.*, vol. 90, no. 4, pp. 524–534, Apr. 2004.

[8] L. Bruzzone, D. F. Prieto, and S. B. Serpico, "A neural-statistical approach to multitemporal and multisource remote-sensing image classification," *IEEE Trans. Geosci. Remote Sens.*, vol. 37, no. 3, pp. 1350–1359, May 1999.

[9] F. Melgani, "Classification of multitemporal remote-sensing images by a fuzzy fusion of spectral and spatio-temporal contextual information," *Int. J. Pattern Recognit. Artif. Intell.*, vol. 18, no. 2, pp. 143–156, 2002.

[10] F. Melgani and S. B. Serpico, "A statistical approach to the fusion of the spectral and spatio-temporal contextual information for the classification of remote sensing images," *Pattern Recognit. Lett.*, vol. 23, no. 9, pp. 1053–1061, Jul. 2002.

[11] K. Conradsen, A. Aasbjerg Nielsen, J. Schou, and H. Skriver, "A test statistic in the complex Wishart distribution and its application to change detection in polarimetric SAR data," *IEEE Trans. Geosci. Remote Sens.*, vol. 41, no. 1, pp. 4–19, Jan. 2003.

[12] P. Lombardo and T. Macrí Pellizzeri, "Maximum likelihood signal processing techniques to detect a step pattern of change in multitemporal SAR images," *IEEE Trans. Geosci. Remote Sens.*, vol. 40, no. 4, pp. 853–870, Apr. 2002.

[13] A. Singh, "Digital change detection techniques using remotely-sensed data," *Int. J. Remote Sens.*, vol. 10, no. 6, pp. 989–1003, 1989.

[14] S. C. Liew, S.-P. Kam, T.-P. Tuong, P. Chen, V. Q. Minh, and H. Lim, "Application of multitemporal ERS-1 synthetic aperture radar in delineating rice cropping systems in the Mekong River Delta, Vietnam," *IEEE Trans. Geosci. Remote Sens.*, vol. 36, no. 5, pp. 1412–1420, Sep. 1998.

[15] W. Dierking and H. Skriver, "Change detection for thematic mapping by means of airborne multitemporal polarimetric SAR imagery," *IEEE Trans. Geosci. Remote Sens.*, vol. 40, no. 3, pp. 618–636, Mar. 2002.

[16] J. Kittler and J. Illingworth, "Minimum error thresholding," *Pattern Recognit.*, vol. 19, no. 1, pp. 41–47, 1986.

[17] F. Melgani, G. Moser, and S. B. Serpico, "Unsupervised change detection methods for remote sensing images," *Opt. Eng.*, vol. 41, no. 12, pp. 3288–3297, Dec. 2002.

[18] G. Moser, F. Melgani, and S. B. Serpico, "Advances in unsupervised change detection," in *Frontiers of Remote Sensing Information Processing*, C. H. Chen, Ed. Singapore: World Scientific, 2003.

[19] G. Moser, J. Zerubia, and S. B. Serpico, "SAR amplitude probability density function estimation based on a generalized Gaussian model," *IEEE Trans. Image Process.*, vol. 15, no. 6, pp. 1429–1442, Jun. 2006.

[20] C. Tison, J.-M. Nicolas, F. Tupin, and H. Maitre, "A new statistical model for Markovian classification of urban areas in high-resolution SAR images," *IEEE Trans. Geosci. Remote Sens.*, vol. 42, no. 10, pp. 2046–2057, Oct. 2004.

[21] Y. Bazi, L. Bruzzone, and F. Melgani, "An unsupervised approach based on the generalized Gaussian model to automatic change detection in multitemporal SAR images," *IEEE Trans. Geosci. Remote Sens.*, vol. 43, no. 4, pp. 874–887, Apr. 2005.

[22] H. L. Van Trees, *Detection, Estimation and Modulation Theory*, vol. 1. Hoboken, NJ: Wiley, 1968.

[23] A. Papoulis, *Probability, Random Variables, and Stochastic Processes*, 3rd ed. New York: McGraw-Hill, 1991.

[24] J. Villasenor, D. Fatland, and L. Hinzman, "Change detection on Alaska's north slope using repeat-pass ERS-1 SAR images," *IEEE Trans. Geosci. Remote Sens.*, vol. 31, no. 1, pp. 227–236, Jan. 1993.

[25] J. S. Lee, K. W. Hoppel, S. A. Mango, and A. R. Miller, "Intensity and phase statistics of multilook polarimetric and interferometric SAR imagery," *IEEE Trans. Geosci. Remote Sens.*, vol. 32, no. 5, pp. 1017–1028, Sep. 1994.

[26] W. Rudin, *Principles of Mathematical Analysis*, 2nd ed. New York: McGraw-Hill, 1976.

[27] I. Sneddon, *The Use of Integral Transforms*. New York: McGraw-Hill, 1972.

[28] G. Moser, J. Zerubia, and S. B. Serpico, "Dictionary-based stochastic expectation-maximization for SAR amplitude probability density function estimation," *IEEE Trans. Geosci. Remote Sens.*, vol. 44, no. 1, pp. 188–200, Jan. 2006.

[29] J. M. Nicolas, "Introduction aux statistiques de deuxième espéce: Application aux lois d'images RSO (Introduction to second kind statistics: Applications to SAR images laws)," ENST, Paris, France, Res. Rep. 2002D001, Feb. 2002, (in french).

[30] E. E. Kuruoglu and J. Zerubia, "Modeling SAR images with a generalization of the Rayleigh distribution," *IEEE Trans. Image Process.*, vol. 13, no. 4, pp. 527–533, Apr. 2004.

[31] W. H. Press, S. A. Teukolsky, W. T. Wetterling, and B. P. Flannery, *Numerical Recipes in C*. Cambridge, U.K.: Cambridge Univ. Press, 2002.

[32] A. Tesei and C. S. Regazzoni, "HOS-based generalized noise PDF models for signal detection optimization," *Signal Process.*, vol. 65, no. 2, pp. 267–281, Mar. 1998.

[33] A. P. Dempster, N. M. Laird, and D. B. Rubin, "Maximum likelihood from incomplete data and the EM algorithm," *J. R. Statist. Soc.*, vol. 39, no. 1, pp. 1–38, 1977.

[34] G. Celeux, D. Chauveau, J. Diebolt, "On stochastic versions of the EM algorithm," INRIA, Le Chesnay, France, Res. Rep. 2514, Mar. 1995. [Online]. Available: http://www.inria.fr/rrrt/rr-2514.html

[35] Y. Delignon, A. Marzouki, and W. Pieczynski, "Estimation of generalized mixtures and its application to image segmentation," *IEEE Trans. Image Process.*, vol. 6, no. 10, pp. 1364–1375, Oct. 2001.

Gabriele Moser (S'03–M'05) received the laurea (M.S.) degree in telecommunications engineering (*summa cum laude*) and the Ph.D. degree in space sciences and engineering from the University of Genoa, Genoa, Italy, in 2001 and 2005, respectively.

Since 2001, he has been cooperating with the Signal Processing and Telecommunications Research Group, Department of Biophysical and Electronic Engineering (DIBE), University of Genoa, in the field of remote-sensing image analysis. He is currently a Research Fellow at DIBE. From January to March 2004, he was a Visiting Student at the Institut National de Recherche en Informatique et en Automatique, Sophia Antipolis, France, working with the "Ariana" Research Group on the problem of synthetic aperture radar (SAR) data modeling. His research activity is focused on image-processing and image-analysis methodologies for remote-sensing data interpretation. His research interests include SAR data analysis, multitemporal image classification, partially supervised classification, hyperspectral image analysis, and contextual classification. He is a reviewer for several international journals.

Sebastiano B. Serpico (M'97–SM'00) received the laurea degree in electronic engineering and the Ph.D. degree in telecommunications from the University of Genoa, Genoa, Italy, in 1982 and 1989, respectively.

Since 1982, he has been cooperating with the Department of Biophysical and Electronic Engineering (DIBE), University of Genoa, in the field of image processing and recognition. He was an Assistant Professor from 1990 to 1998, an Associate Professor from 1998 to 2004, and a Full Professor of telecommunications with the Faculty of Engineering, University of Genoa, where he taught signal theory, pattern recognition, telecommunication systems, and electrical communications. From 1995 to 1998, he was the Head of the Signal Processing and Telecommunications Research Group (SP&T) of DIBE, University of Genoa, and is currently the Head of the SP&T Laboratory. He is the Chairman of the Institute of Advanced Studies in Information and Communication Technologies. His current research interests include the application of pattern recognition (feature selection, classification, change detection, and data fusion) to remotely sensed images. He is the author or coauthor of more than 150 scientific publications, including journals and conference proceedings.

Dr. Serpico was the recipient of the Recognition of TGARS Best Reviewers from the IEEE Geoscience and Remote Sensing Society in 1998. He coedited a Special Issue (July 2001) of the IEEE TRANSACTIONS ON GEOSCIENCE AND REMOTE SENSING on the subject of the analysis of hyperspectral image data and a Special Issue (March 2005) on the advances in techniques for the analysis of remotely sensed data. Since 2001, he has been an Associate Editor of the IEEE TRANSACTIONS ON GEOSCIENCE AND REMOTE SENSING. He is a member of the International Association for Pattern Recognition.